

Article

X-ray Phase-Contrast Computed Tomography for Soft Tissue Imaging at the Imaging and Medical Beamline (IMBL) of the Australian Synchrotron

Benedicta D. Arhatari ^{1,2,3,*} , Andrew W. Stevenson ^{1,4} , Brian Abbey ³ , Yakov I. Nesterets ^{4,5}, Anton Maksimenko ¹, Christopher J. Hall ¹, Darren Thompson ^{4,5} , Sheridan C. Mayo ⁴, Tom Fiala ¹, Harry M. Quiney ², Seyedamir T. Taba ⁶, Sarah J. Lewis ⁶, Patrick C. Brennan ⁶, Matthew Dimmock ⁷ , Daniel Häusermann ¹ and Timur E. Gureyev ^{2,5,6,7}

- ¹ Australian Synchrotron, ANSTO, Clayton, VIC 3168, Australia; stevensa@ansto.gov.au (A.W.S.); antonm@ansto.gov.au (A.M.); christoh@ansto.gov.au (C.J.H.); tomf@ansto.gov.au (T.F.); danielh@ansto.gov.au (D.H.)
- ² School of Physics, The University of Melbourne, Parkville, VIC 3010, Australia; quiney@unimelb.edu.au (H.M.Q.); timur.gureyev@unimelb.edu.au (T.E.G.)
- ³ Department of Chemistry and Physics, La Trobe University, Bundoora, VIC 3086, Australia; B.Abbey@latrobe.edu.au
- ⁴ CSIRO, Clayton, VIC 3168, Australia; Yakov.Nesterets@csiro.au (Y.I.N.); Darren.Thompson@csiro.au (D.T.); Sherry.Mayo@csiro.au (S.C.M.)
- ⁵ School of Science and Technology, University of New England, Armidale, NSW 2351, Australia
- ⁶ Faculty of Medicine and Health, University of Sydney, Sydney, NSW 2006, Australia; amir.tavakoli@sydney.edu.au (S.T.T.); sarah.lewis@sydney.edu.au (S.J.L.); patrick.brennan@sydney.edu.au (P.C.B.)
- ⁷ Medical Imaging & Radiation Sciences, Monash University, Clayton, VIC 3168, Australia; matthew.dimmock@monash.edu
- * Correspondence: arhatarb@ansto.gov.au



Citation: Arhatari, B.D.; Stevenson, A.W.; Abbey, B.; Nesterets, Y.I.; Maksimenko, A.; Hall, C.J.; Thompson, D.; Mayo, S.C.; Fiala, T.; Quiney, H.M.; et al. X-ray Phase-Contrast Computed Tomography for Soft Tissue Imaging at the Imaging and Medical Beamline (IMBL) of the Australian Synchrotron. *Appl. Sci.* **2021**, *11*, 4120. <https://doi.org/10.3390/app11094120>

Received: 15 April 2021

Accepted: 28 April 2021

Published: 30 April 2021

Publisher's Note: MDPI stays neutral with regard to jurisdictional claims in published maps and institutional affiliations.



Copyright: © 2021 by the authors. Licensee MDPI, Basel, Switzerland. This article is an open access article distributed under the terms and conditions of the Creative Commons Attribution (CC BY) license (<https://creativecommons.org/licenses/by/4.0/>).

Abstract: The Imaging and Medical Beamline (IMBL) is a superconducting multipole wiggler-based beamline at the 3 GeV Australian Synchrotron operated by the Australian Nuclear Science and Technology Organisation (ANSTO). The beamline delivers hard X-rays in the 25–120 keV energy range and offers the potential for a range of biomedical X-ray applications, including radiotherapy and medical imaging experiments. One of the imaging modalities available at IMBL is propagation-based X-ray phase-contrast computed tomography (PCT). PCT produces superior results when imaging low-density materials such as soft tissue (e.g., breast mastectomies) and has the potential to be developed into a valuable medical imaging tool. We anticipate that PCT will be utilized for medical breast imaging in the near future with the advantage that it could provide better contrast than conventional X-ray absorption imaging. The unique properties of synchrotron X-ray sources such as high coherence, energy tunability, and high brightness are particularly well-suited for generating PCT data using very short exposure times on the order of less than 1 min. The coherence of synchrotron radiation allows for phase-contrast imaging with superior sensitivity to small differences in soft-tissue density. Here we also compare the results of PCT using two different detectors, as these unique source characteristics need to be complemented with a highly efficient detector. Moreover, the application of phase retrieval for PCT image reconstruction enables the use of noisier images, potentially significantly reducing the total dose received by patients during acquisition. This work is part of ongoing research into innovative tomographic methods aimed at the introduction of 3D X-ray medical imaging at the IMBL to improve the detection and diagnosis of breast cancer. Major progress in this area at the IMBL includes the characterization of a large number of mastectomy samples, both normal and cancerous, which have been scanned at clinically acceptable radiation dose levels and evaluated by expert radiologists with respect to both image quality and cancer diagnosis.

Keywords: phase-contrast; computed tomography; soft-tissue imaging; synchrotron

1. Introduction

The Imaging and Medical Beamline (IMBL) at the Australian Synchrotron [1] is a hard X-ray beamline that has facilitated user experiments for more than a decade. Its superconducting multipole wiggler insertion device can produce nearly parallel polychromatic and monochromatic X-ray beams through a double-crystal Laue monochromator (DCLM), with energies ranging from 25 to 120 keV. The IMBL user experimental program encompasses a wide range of applications from materials to life sciences. In the majority of cases, experiments are performed under ambient conditions; however, for some material science applications, the beamline can incorporate specialized sample stages for heating [2], cooling, or performing in-liquid experiments. The sample can also be subjected to in situ loading during measurements, including tensile stress [3], compression, etc. For large, flat, laterally extended objects such as circuit boards or paintings, the nonconventional tomographic technique termed “laminography” can also be used [4]. Several imaging modalities can be utilized at IMBL for both two-dimensional (2D) and/or three-dimensional (3D) imaging, including propagation-based phase-contrast techniques [5,6], grating-based techniques [7], speckle-based techniques [8], scatter-based techniques [9], and dark-field imaging [10]. The choice of technique depends largely on the specific application. Dynamic or high-speed imaging as a function of time [2,11,12] is also possible due to the comparatively high X-ray flux at IMBL. Furthermore, one of the IMBL’s biggest strengths is its potential for medical and biomedical imaging applications, especially in regard to radiotherapy [13–15] and imaging/tomography [6,16,17]. Computed tomography (CT) is a 3D imaging technique [18,19] to image the internal structures of an object without superimposing the layers of the object as in 2D projection images. The beamline is equipped with animal-holding facilities, a PC2-certified wet laboratory, surgical equipment, an anesthesia delivery system, ventilators, a biohazard cabinet, incubators for cell culture, and a cell analyzer [20]. These facilities act as in-house clinics and are important for sample preparation. Because both radiotherapy and imaging/tomography modalities at the IMBL have the potential for preclinical and clinical application development, a dedicated preclinical station including a small-animal irradiation stage is available to users of the beamline. Moreover, a 3D breast CT imaging facility with a rotating patient bed is under development for patient trials in the near future.

There are six hutches at the IMBL in total. Hutches 1A, 2A, and 3A are the beam-conditioning hutches and contain X-ray optical elements. The experiment hutches are 1B, 2B, and 3B, in order of increasing distance from the source. Radiotherapy experiments [13] have mainly been conducted in Hutch 1B or 2B. Imaging and tomography experiments for small samples are conducted in Hutch 2B, while Hutch 3B can be used for imaging samples as large as a human torso due to the very wide (over 50 cm) beam available at that location. Hutch 3B is located in a satellite building, 140 m further away from the source to achieve a wide beam while also allowing for a large (up to 7 m) sample-to-detector distance for propagation-based phase-contrast imaging. A schematic diagram of the key components in these hutches can be found in Stevenson et al. [20].

The interaction between the X-ray beam and the sample can be generally described by the complex refractive index at a given wavelength, $n = 1 - \delta + i\beta$, where δ is related to the phase shift, and β is related to the attenuation. Conventional X-ray projection images primarily depend on the linear attenuation coefficient, $\mu(\lambda) = 4\pi\beta(\lambda)/\lambda$, where λ is the X-ray wavelength. The output intensity, I , in monochromatic case is given by integrating the attenuation through the sample in the direction of X-ray propagation, z , as follows [21]:

$$I = I_0 \exp^{-\int \mu(z) dz} \quad (1)$$

where I_0 is the incident intensity. For low-density materials, such as soft tissue, the X-ray attenuation generates only relatively low contrast [22]. By comparison, in the hard X-ray regime, the phase shift is typically three orders of magnitude larger than the corresponding absorption. This has led to hard X-ray phase-contrast imaging, which utilizes refraction (i.e.,

X-ray phase shifts), becoming an increasingly widespread technique for the nondestructive imaging of low-density samples [23,24]. X-rays that pass through materials undergo a phase shift, $\varphi = -2\pi\delta(\lambda)T/\lambda$, where T is the local sample thickness. Spatial variations of the phase in the object plane affect the intensity in the image plane at a distance z downstream from the object, and can be accurately described by the Transport of Intensity Equation (TIE) [25]:

$$\frac{\partial I(x, y, z)}{\partial z} + \frac{1}{k} \nabla_{\perp} \cdot (I(x, y, z) \nabla_{\perp} \varphi(x, y, z)) = 0 \quad (2)$$

where $k = 2\pi/\lambda$ is the wavenumber, and ∇_{\perp} is the 2D differential operator in the plane perpendicular to the optical axis, z . The free-space propagation-based phase-contrast imaging method described by the TIE equation is often easier to implement compared to other phase-sensitive X-ray imaging techniques, due to its straightforward experimental setup, which does not require any optical elements [26,27]. This method simply allows a spatially coherent wave field to propagate a sufficient distance away from the sample so that the diffraction fringes can be observed. Due to its simplicity, this propagation-based contrast mechanism may be readily applied to 3D CT imaging [5,28,29]. In propagation-based phase-contrast computed tomography (PCT), an additional step (compared to conventional absorption-based tomography) is required, during which a suitable phase-retrieval algorithm is applied to the measured intensity to retrieve the phase shifts induced by the sample. There are several approaches that are currently used to solve the phase-retrieval problem for propagation-based contrast in the measured intensity. The method chosen often depends on the imaging regime within which the data has been acquired. Phase retrieval based on the TIE [27,30] is primarily used for quantitative phase imaging in the near-field Fresnel region. For homogeneous samples, the “homogeneous” TIE-based phase retrieval (“TIE-Hom”) [31] algorithm (also known as Paganin’s method) can be applied to each measured 2D propagation-based phase-contrast intensity image, as follows (note that z is fixed) [31]:

$$T(x, y) = -\ln \left[\mathbb{F}^{-1} \left(\frac{\lambda}{4\pi\beta + z\delta\lambda u^2} \mathbb{F} \left[\frac{I(x, y, z)}{I_0} \right] \right) \right] \quad (3)$$

where $u = (u_x, u_y)$ is the Fourier conjugate of (x, y) , \mathbb{F} is the Fourier transform operation, and \mathbb{F}^{-1} is the inverse Fourier transform. The TIE-Hom algorithm is particularly useful for imaging approximately homogeneous low-density objects. However, it can also be applied to objects consisting of several different components with similar X-ray attenuation properties such as breast tissue (which mainly consists of adipose and glandular tissues) [5,32]. This is due to the fact that TIE-Hom acts as a low-pass filter, and the ratio δ/β effectively determines the resultant image sharpness. Moreover, for samples containing two homogeneous materials (denoted by 1 and 2), one can justifiably use the ratio of the differences $(\delta_1 - \delta_2)/(\beta_1 - \beta_2)$, as described by Beltran et al. [33] and Nesterets et al. [34]. The TIE-Hom PCT technique is practicable for biomedical CT imaging as it requires only one projection at each viewing angle to be collected at a single propagation distance. Alternative two-plane TIE-based phase-retrieval approaches [27,35] would have a distinct disadvantage for this application. They would result in doubling the dose received by the sample, as it requires two images per projection. In addition, the precise alignment of the two images collected at different propagation distances, required by this method, would likely be creating another problem as it is not a simple task.

Breast cancer is one of the two leading causes of cancer-related deaths in the world. The success of breast cancer treatment relies on early detection [36]. Currently, the primary screening method for breast cancer detection is mammography, which produces a 2D image. However, a fundamental limitation in mammography results from the superposition of breast tissue layers within 2D projection images, which potentially obscures fine details and produces errors in diagnosis [32]. On the other hand, 3D imaging techniques such as breast CT are not yet well-established in medical practice due to the issues related to the relatively high radiation doses required. The objective of the current study is thus to explore novel

methods of imaging that minimize the dose to the patient while simultaneously enhancing image quality in a way that can be applied in clinical practice.

The focus of the current paper is on the current state and progress of propagation-based PCT imaging at the IMBL, which has been found to be highly efficient for low-density samples such as breast and other soft tissues [5,37]. Phase-contrast imaging has been shown to significantly increase contrast in soft tissue under suitable experimental conditions [38]. Biomedical samples are often very sensitive to radiation, which means that the X-ray doses must be carefully controlled. Another significant benefit of the TIE-Hom phase-retrieval algorithm is that it improves the signal-to-noise ratio (SNR) [34,39,40], enabling the radiation dose delivered to soft tissue to be reduced while still producing high-quality images.

2. Materials and Methods

The propagation-based PCT experiments reported in this article were performed in hutch 3B with a source-to-sample distance of 137 m and a sample-to-detector distance of 0.19 m (this is the minimum practically achievable distance for absorption contrast) and 6 m (phase contrast). Figure 1 illustrates the schematic diagram of the experimental setup. The large distance between the sample and detector allows the propagation-based X-ray phase contrast to be observed [5,24,41]. The experiments were performed at a wiggler magnetic field of 3 Tesla with the following in-vacuum filters: C(0.45), C[hd](5), C[hd](10), Al(1)-Al(1), and Al(1)-Al(1) (all but the C(0.45) filter are at 45°). The experiments were conducted with monochromatic X-rays at the energies of 26, 28, 32, and 34 keV. Unlike the polychromatic X-rays in the clinical instruments that contain a broad spectrum with the disadvantage that the lower-energy component contributes more to the patient dose, monochromatic X-rays help to minimize the patient dose. To flatten the beam in the vertical direction, the DCLM was set at an appropriate bending configuration. First crystal benders were set to 2.01 and second crystal benders were set to 1.84. These values refer to the ratio of the source to crystal distance and the bending radius. Due to the low dose requirement for the breast tissue samples, detuning of the DCLM was applied in order to move away from the Bragg peak position. The beam size in the sample plane was 20 cm (horizontally) × 4 cm (vertically).

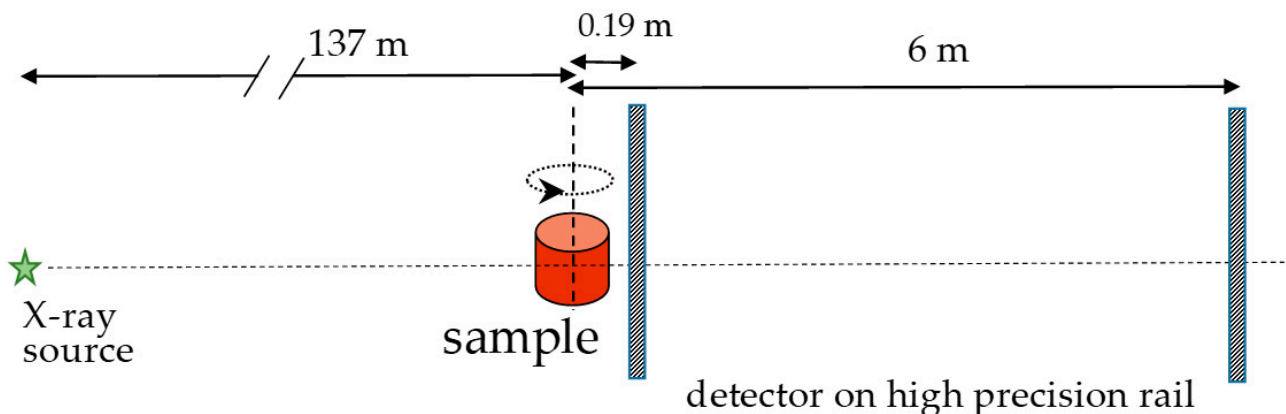


Figure 1. Schematic diagram of the experimental setup for absorption-contrast CT (detector at 0.19 m) and propagation-based PCT (detector at 6 m).

The samples were fresh full-breast mastectomies that were obtained from breast cancer surgery operations and were imaged at the IMBL on the same day in a complete, intact, and unfixed state. No additional sample preparation was applied prior to scanning. However, before and after scanning, samples were handled inside a biosafety cabinet (Level 1), and the appropriate biosafety procedures were followed when the samples were placed inside or removed from the sealed 11 cm diameter plastic cylinders (used for sample storage) for

the PCT scans. The sample was positioned vertically inside the plastic cylinder along the direction from the nipple (top) to the pectoralis major (bottom). Most samples contained different types and grades of breast cancer lesions, but as a control, we also received and imaged cancer-free samples from prophylactic surgery. The imaging experiments were conducted under a Human Ethics Certificate of Approval from Monash University (Project ID 26399) and with written consent from the patients to image their clinical specimens. For evaluation and quantification of the detector resolution, we used a resolution test phantom target (QRM-D100-HCR, QRM GmbH, Möhrendorf, Germany). The phantom was composed of materials designed to mimic soft tissue and had an overall diameter of 10 cm and incorporated line patterns of different sizes.

The samples were exposed to X-rays under clinically relevant mean glandular doses (MGD) of 2, 4, and 8 mGy (the 8 mGy MGD was above the dose used under actual clinical conditions but was included for comparison purposes). The MGD was determined for a breast composed of 30% glandular and 70% adipose tissue. Before the experiment, an ion chamber was installed in the X-ray beam to calibrate the detected flux at the detector by adjusting the rocking angle $\Delta\theta$ of the monochromator to control the incident photon fluence. To this end, the ion chamber readings and the corresponding detector readings were collected for two sample-to-detector distances, 0.19 and 6 m. Ion chamber readings were used to estimate the corresponding MGD using Monte Carlo simulations for a numeric breast phantom with a diameter of 11 cm [5,32,34]. Finally, the averaged flat-field (sample-free) signal at the detector was tabulated as a function of MGD for several experimental conditions, including X-ray energy, sample-to-detector distance, and for different detectors. After the MGD calibration, the ion chamber was removed from the X-ray beam and was not used during the tomographic scanning of samples (the width and height of the ion chamber acceptance are smaller than the corresponding dimensions of the X-ray beam and the samples).

Breast tissue imaging at IMBL was conducted on an approximately weekly basis to correlate with the breast surgeries at Monash Health, Victoria, Australia. All the necessary set-up configurations were standardized using a suite of purpose-designed computer scripts to maintain the same experimental conditions for every sample. This included setting the slit positions, detector position, sample position, incident energy setting from the monochromator, etc. Each tomographic scan was performed by rotating the sample over a 180° range. The scan data consisted of 4800 projections with a step angle of 0.0375° with a corresponding MGD of 8 mGy. A total of 100 dark-current images and 100 flat-field images were collected before each scan to account for the nonuniformity of the imaging system. The dark-current images were collected without X-rays. Flat-field images were collected with the X-ray illumination on but without a sample within the field of view (FOV). From one set of collected data, we produced three sets of reconstruction results: the original 8 mGy MGD result (4800 projections, step angle = 0.0375°), a 4 mGy MGD result using half the number of projections (2400 projections, step angle = 0.075°), and a 2 mGy MGD result using a quarter of the projections (1200 projections, step angle = 0.15°).

The distinctive properties of synchrotron X-ray sources, such as high coherence, energy tunability, and high brightness are very important for producing PCT scans with short exposure times. These source characteristics need to be complemented with a highly efficient detector having a high frame rate, high spatial resolution, high detection efficiency, large area, and low noise level in order to maximize the image quality at the minimal possible radiation dose to the sample. The first X-ray detector used at the IMBL for these scans included a large-area flat-panel imaging detector, the Hamamatsu complementary metal-oxide-semiconductor (CMOS) C10900D with a Cesium Iodide (CsI) scintillator deposited directly on 2D photodiode array with a pixel size of $100\ \mu\text{m} \times 100\ \mu\text{m}$ and a FOV of 12.16 cm (horizontal) \times 12.32 cm (vertical). A second detector was also used in this study in order to compare and contrast the optimal detector characteristics in the context of PCT for soft-tissue imaging. The second detector was a Xineos 3030HR CMOS flat-panel detector with a medical-grade columnar CsI scintillator with a pixel size of $99\ \mu\text{m} \times 99\ \mu\text{m}$.

Both the Hamamatsu and Xineos detectors have a high quantum efficiency and very low noise level, which is important for low-dose PCT scans with short exposure times. The main specifications of both detectors can be seen in Table 1.

Table 1. Detector specifications for the Hamamatsu C10900D [42] and the Xineos 3030HR [43].

	Hamamatsu	Xineos
		
Number of pixels	1216 × 1232	2097 × 2111
Pixel size	100 μm	99 μm
Exposure time	59 ms	25 ms
Frame rate	17 fps	40 fps
Max counts	4000 (12-bit)	16,000 (14-bit)
Acquisition mode	Fine mode	Mag1 (70%)

Note that the Xineos frame rate is available in 3 different modes, i.e., Mag0 (100%—31 fps), Mag1 (70%—40 fps), or Mag2 (50%—54 fps) [43].

Preprocessing of the projection data is required prior to 3D reconstructions. This includes the correction for the dark-current and flat-field images and geometrical correction of the images to account for the gaps between pixel rows or columns and to mask defects in the detector pixels. Both detectors had intermodular gaps or defect lines in both the horizontal and vertical directions that created intensity artefacts in the images. These intensity artefacts need to be corrected in the projection images to prevent them from producing strong ring artefacts in the reconstructed images. Stitching of the projection images in the vertical direction is also necessary for large samples when the height of the sample (in the direction from the nipple to the pectoralis major) exceeds the vertical beam size of 4 cm. Hence, for large samples, we need to take several steps in the vertical direction in order to capture the whole sample. We note that the MGD is higher in the overlap region of the vertically offset images, resulting in a doubling of the dose within this region. However, for future measurements involving patients, we will eliminate the need for any image overlap. The preprocessing and the stitching steps (using the IMBL_Preproc software developed privately by Y.I.N. and D.T. for the breast CT project) were applied to each projection image. The X-TRACT software package [44] was used for data reconstruction, including the phase-retrieval step. The TIE-Hom phase-retrieval algorithm was applied to the projection data set, in order to exploit the phase information, using a δ/β ratio applicable for the relevant materials. For each energy, the ratio δ/β was calculated with respect to the glandular and tumor tissues ($(\delta_{gland} - \delta_{tm})/(\beta_{gland} - \beta_{tm}) = 399, 452, 550, \text{ and } 600$ for X-ray energy at 26, 28, 32, and 34 keV, respectively). While differentiating glandular and adipose tissues in CT slices is relatively easy, we are mainly interested in differentiating glandular and cancerous tissues. It turns out that the “relative” δ/β for the latter is smaller than for glandular/adipose and hence should be used if one is interested in observing glandular/tumor interfaces without excessive blurring. If, however, glandular/adipose or tumor/adipose interfaces are of interest, one should use the corresponding “relative” δ/β . The Gridrec algorithm [45] was used for the CT reconstruction of the data reported in this article. An implementation of the Gridrec algorithm and a ring artefact removal filter are also available in the X-TRACT software package. Image data were stored in the interactive computing environment Australian Synchrotron Computer Infrastructure (ASCI) that provided high-performance computing resources [46]. ASCI can be used to analyze users’ data in real time while at the beamline and/or after their beam time by logging in remotely. ASCI provides a convenient web-based interface to launch Linux desktops on high-performance computer hardware.

3. Results

3.1. X-ray Phase-Contrast CT Results

Analysis of the data that have been published previously [32,37,47] demonstrated that the propagation-based PCT technique offers superior soft tissue and tumor visibility compared to the standard absorption-based CT technique. The overall radiological quality evaluation from our studies comparing PCT and standard absorption-based CT are published in Taba et al. [47] for 12 samples and in Gureyev et al. [37] for another 14 samples. PCT images from a variety of mastectomy samples were evaluated and scored by medical imaging specialists and practicing radiologists. The scoring was conducted to evaluate the overall radiological image quality [37,47] for two sample-to-detector distances, 0.19 and 6 m, and varying X-ray energies at certain MGD values. The previous studies show that the PCT images obtained positive scores, which means that the PCT images show higher image quality than the absorption-based CT. On the contrary, a negative score means that the absorption-based CT is better. Additionally, the advanced step of phase retrieval (TIE-Hom algorithm) in the CT reconstruction process has been shown to increase the SNR in the resultant 3D PCT images.

Figure 2 shows the difference between the reconstructed slices from absorption-based CT collected within the contact regime (0.19 m sample-to-detector distance) and the propagation-based PCT slices collected at a 6 m sample-to-detector distance for data taken at 32 keV and 4 mGy MGD. We can see that PCT using TIE-Hom phase retrieval shows better SNR compared to the absorption-based CT. All data presented here was acquired using the Hamamatsu detector. Figure 3 shows the reconstructed slices illustrating the effect of the X-ray energy variation in PCT. The mastectomy sample contained more dense glandular tissue (white color) and less dense adipose tissue (gray color). The glandular tissue yields higher contrast at 34 keV, but the adipose tissue has better contrast using lower energies such as 32 keV. The effect of the MGD variation on the PCT image quality is shown in Figure 4. The highest dose of 8 mGy produced the best results. However, in a clinical setting the lowest achievable dose while maintaining an acceptable image quality is typically required.

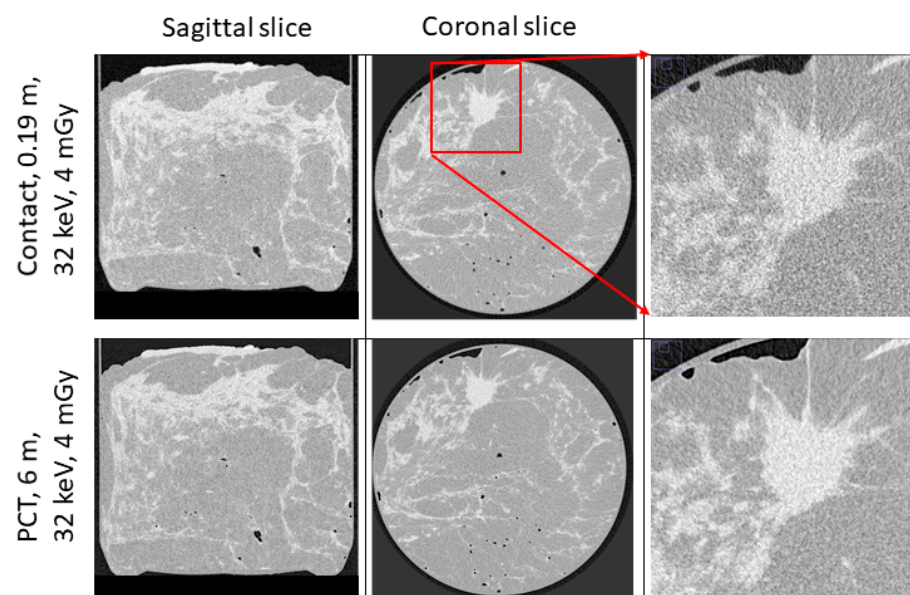


Figure 2. Comparison of absorption-contrast CT at 0.19 m sample-detector distance (top row) with PCT using TIE-Hom phase-retrieval images at a 6 m sample-detector distance (bottom row) of a breast tissue sample. The PCT images exhibit a better signal-to-noise ratio compared to the contact image.

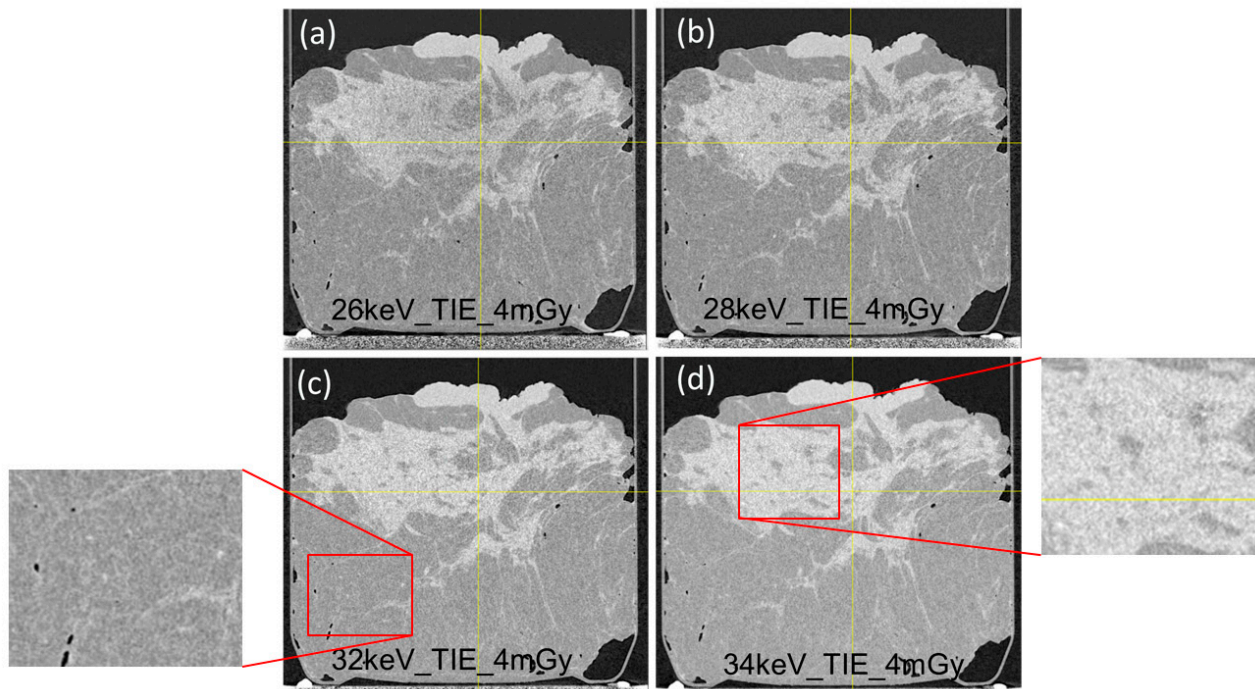


Figure 3. Comparison of PCT images of a breast tissue sample from a sagittal slice obtained using four different X-ray energies: (a) 26, (b) 28, (c) 32, and (d) 34 keV. For the dense glandular component (white color), the result from 34 keV shows the best quality, while 32 keV produces the best quality for the adipose component (gray color).

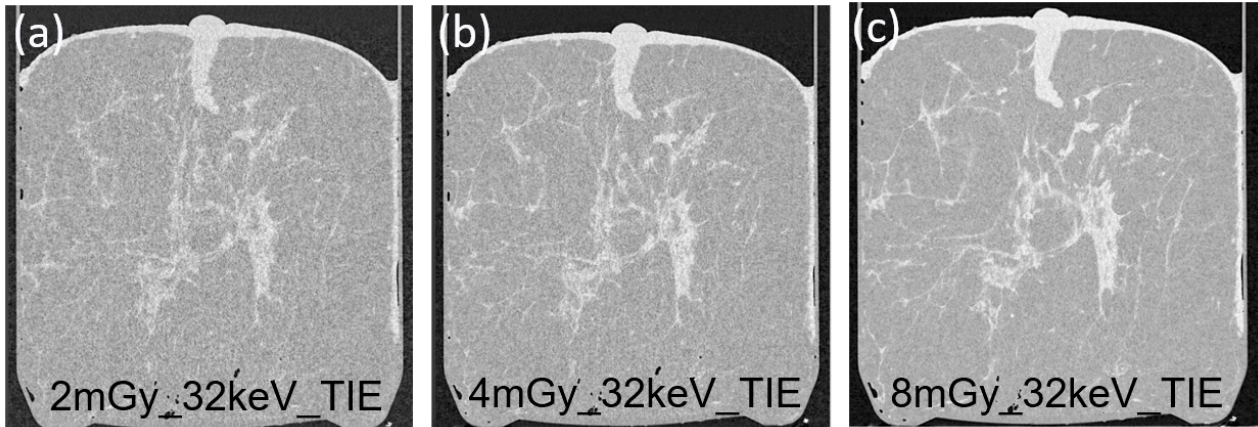


Figure 4. Comparison of PCT images of a breast tissue sample from a sagittal slice obtained with different MGD values: (a) 2, (b) 4, and (c) 8 mGy.

3.2. Detector Comparison

This section presents a comparison of the performance of the two detectors used at the IMBL (Hamamatsu and Xineos) in the context of PCT imaging. Both the Hamamatsu and the Xineos detectors have high quantum efficiency and a very low noise level, which is important for this type of imaging, i.e., low-dose PCT scans with short exposure times. The images produced by the Hamamatsu and the Xineos detectors are shown in Figure 5. Both detectors produced similar-quality images.

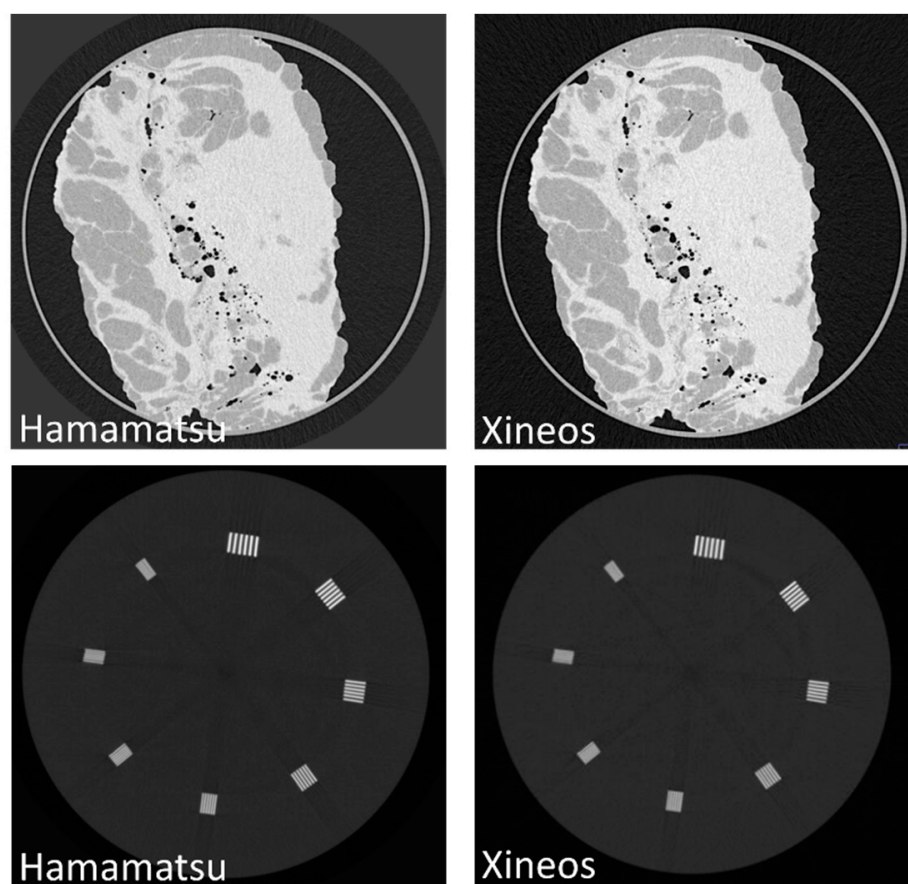


Figure 5. Comparison between images produced by the Hamamatsu (left column) and the Xineos (right column) detectors at 32 keV (6 m distance, 4 mGy) of a breast tissue sample inside an 11 cm diameter plastic container (top row) and a resolution test phantom (bottom row).

Image Quality Assessment

The objective image quality shown in the PCT reconstructions of the breast tissue (see Figure 5, top row) using both detectors was evaluated with several metrics, including the intrinsic spatial resolution of the reconstructed slice, SNR, and the ratio of the SNR to the average spatial resolution (SNR/res) [40]. These measurements were carried out using the X-TRACT software within small uniform regions selected in the images. The intrinsic spatial resolution is estimated in X-TRACT by calculating the noise power spectrum within these uniform regions and evaluating the inverse of the square root of the second moment of that spectrum. Further details of the resolution calculations using X-TRACT can be found in Nesterets et al. [5] and Gureyev et al. [48]. These measurements were carried out at every tenth slice from the 3D reconstruction stacks with 280 slices in total yielding ten resultant values from the central region of the CT stack. The intrinsic spatial resolution was systematically measured as x_{res} and y_{res} in two orthogonal directions of the reconstructed slices. This measurement was performed in the adipose and glandular regions separately by averaging over the values from the ten slices from the CT stack. The results are presented in Table 2. In the case of the Hamamatsu detector, a spatial resolution of $150 \mu\text{m} \times 174 \mu\text{m}$ was determined predominantly by the detector's point-spread function. Similar spatial resolution anisotropy was also observed in the Xineos detector: $167 \mu\text{m} \times 185 \mu\text{m}$. Furthermore, we saw a typical trade-off that the Hamamatsu detector produced slightly better spatial resolution than the Xineos detector; however, the Xineos detector produced slightly better values of SNR/res than the Hamamatsu detector.

Table 2. Measured spatial resolution, SNR, and SNR/res for the PCT images produced using data from the Hamamatsu and the Xineos detectors, respectively, of the adipose and glandular tissues in a mastectomy sample scanned at 32 keV (6 m sample-detector distance, MGD = 4 mGy).

	Adipose		Glandular	
	Hamamatsu	Xineos	Hamamatsu	Xineos
x_{res} (μm)	152 ± 9	169 ± 7	147 ± 4	164 ± 2
y_{res} (μm)	172 ± 11	183 ± 7	175 ± 6	186 ± 5
SNR	6.0 ± 0.6	7.6 ± 0.5	7.4 ± 0.9	9.3 ± 0.3
SNR/res (μm^{-1})	0.037 ± 0.004	0.043 ± 0.002	0.046 ± 0.006	0.053 ± 0.002

To further compare the image quality, the visibility of the images produced by the two detectors was evaluated. Visibility was defined as the ratio of the difference between the maximum (*max*) and minimum (*min*) values in the reconstructed image divided by their sum, as first formulated by Michelson [49], using the following equation:

$$V = \frac{\text{max} - \text{min}}{\text{max} + \text{min}} \quad (4)$$

The line pattern visibility was calculated for the PCT images collected with the resolution test phantom as shown in Figure 5 (bottom row) by averaging over five repeated measurement visibility values. The measurement error of ± 0.02 was calculated from the standard deviation of these five values. The line pattern visibility plot is presented in Figure 6 as a function of spatial frequency (line pairs per centimeter). The visibility performance of both detectors was comparable, with the Xineos detector producing slightly better image visibility in the range of 10 to 20 lp/cm.

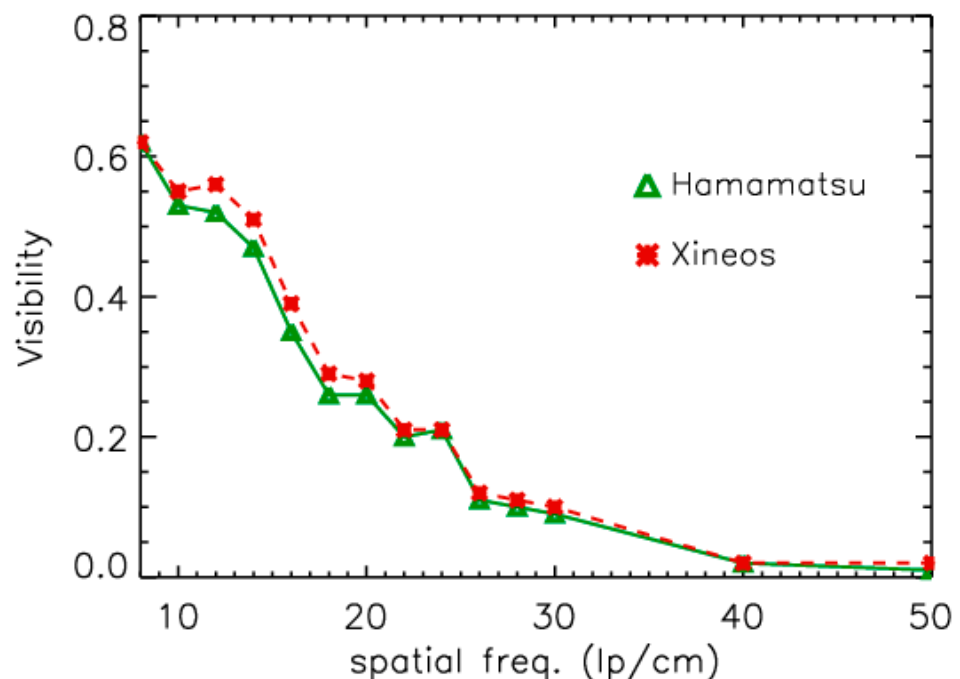


Figure 6. Comparison of the line pattern visibility for PCT images obtained using data from the Hamamatsu and the Xineos detectors as a function of the spatial frequency of the resolution test phantom (expressed as line pairs/cm).

Both detectors produced images with comparable quality. However, the Xineos detector provided additional benefits in terms of a larger FOV and faster frame rate (40 fps)

compared to Hamamatsu. Moreover, the frame rate of the Xineos detector can be further increased, in its Mag2 (50%) imaging mode, to a maximum of 54 fps.

4. Conclusions

The IMBL at the ANSTO Australian Synchrotron is well suited to propagation-based phase-contrast computed tomography imaging of biological samples such as excised mastectomies at low radiation doses, such as 2 mGy. With the help of the phase-retrieval TIE-Hom algorithm, the SNR is found to be enhanced, allowing the low-dose imaging of soft tissues while still producing high-quality, clinically-relevant results. Therefore, it is expected that propagation-based PCT will be incorporated into medical breast imaging at the IMBL in the near future providing higher tissue contrast and a better signal-to-noise ratio than is currently possible with conventional absorption-based imaging. Crucially, PCT also potentially reduces the radiation dose delivered to the patient and avoids the need for painful breast compression that is required as part of the current approaches to 2D mammography. With the combination of a highly efficient, high frame rate detector, a full PCT data set with 150 μm spatial resolution and sufficiently high SNR can be collected in less than 1 min, e.g., 30 s for 1200 projections using the Xineos detector, or 71 s using 1200 projections for the Hamamatsu detector. The comparison between the Hamamatsu and the Xineos detectors shows that images of comparable quality can be obtained using either detector. Slightly better spatial resolution was obtained with the Hamamatsu, while better SNR/resolution was achieved with the Xineos. The user can quickly process the collected data during the beam time or access the data after the beam time using the ASCI desktop high-performance computing facility. In the future, higher-resolution PCT will be possible, albeit for smaller samples, using the new Micro-Computed Tomography (MCT) beamline, which is currently being constructed as part of the BRIGHT program at the Australian Synchrotron. The new MCT beamline will be used for high-resolution computed tomography and provide complementary information to the IMBL beamline.

Author Contributions: All authors contributed significantly to this work. B.D.A., A.W.S., B.A., Y.I.N., S.J.L., P.C.B., M.D., D.H., T.E.G. wrote the manuscript, Y.I.N., A.M., C.J.H., H.M.Q., S.T.T., S.J.L., P.C.B., D.H., T.E.G. designed experiments, B.D.A., Y.I.N., A.M., C.J.H., D.T., S.C.M., T.F., M.D., T.E.G. performed experiments, B.D.A., Y.I.N., D.T., T.E.G., S.T.T. analysed data. All authors have read and agreed to the published version of the manuscript.

Funding: This research was funded by NHMRC Australia, Project Grant 1138283 “Towards the clinical application of phase-contrast computed tomography in breast cancer imaging” and ANSTO project funding.

Institutional Review Board Statement: The imaging experiment was conducted under a Human Ethics Certificate of Approval from Monash University (project ID 26399) and with written consent from the patients.

Informed Consent Statement: Informed consent was obtained from all subjects involved in the study.

Data Availability Statement: The data presented in this study are available on request from the corresponding author.

Acknowledgments: We acknowledge the support of J. Fox, B. Kumar, and Z. Prodanovic from Monash University, Australia, in providing the mastectomy samples for this study. Special thanks to the individuals who consented to having their mastectomies used for research purposes in this study.

Conflicts of Interest: The authors declare no conflict of interest.

References

1. Boldeman, J.W.; Einfeld, D. The physics design of the Australian synchrotron storage ring. *Nucl. Instrum. Methods Phys. Res. A* **2004**, *521*, 306–317. [[CrossRef](#)]
2. Mayo, S.C.; McCann, T.; Day, L.; Favaro, J.; Tuhumury, H.; Thompson, D.; Maksimenko, A. Rising dough and baking bread at the Australian synchrotron. *AIP Conf. Proc.* **2016**, *1696*, 020006. [[CrossRef](#)]

3. Thornton, J.; Arhatari, B.D.; Sesso, M.; Wood, C.; Zonneveldt, M.; Kim, S.Y.; Kimpton, J.A.; Hall, C. Failure Evaluation of a SiC/SiC Ceramic Matrix Composite During In-Situ Loading Using Micro X-ray Computed Tomography. *Microsc. Microanal.* **2019**, *25*, 583–591. [[CrossRef](#)]
4. van Aarle, W.; Palenstijn, W.J.; Cant, J.; Janssens, E.; Bleichrodt, F.; Dabrovolski, A.; De Beenhouwer, J.; Joost Batenburg, K.; Sijbers, J. Fast and flexible X-ray tomography using the ASTRA toolbox. *Opt. Express* **2016**, *24*, 25129–25147. [[CrossRef](#)] [[PubMed](#)]
5. Nesterets, Y.I.; Gureyev, T.E.; Mayo, S.C.; Stevenson, A.W.; Thompson, D.; Brown, J.M.; Kitchen, M.J.; Pavlov, K.M.; Lockie, D.; Brun, F.; et al. A feasibility study of X-ray phase-contrast mammographic tomography at the Imaging and Medical beamline of the Australian Synchrotron. *J. Synchrotron Radiat.* **2015**, *22*, 1509–1523. [[CrossRef](#)]
6. Stevenson, A.W.; Mayo, S.C.; Hausermann, D.; Maksimenko, A.; Garrett, R.F.; Hall, C.J.; Wilkins, S.W.; Lewis, R.A.; Myers, D.E. First experiments on the Australian Synchrotron Imaging and Medical beamline, including investigations of the effective source size in respect of X-ray imaging. *J. Synchrotron Radiat.* **2010**, *17*, 75–80. [[CrossRef](#)]
7. Morgan, K.S.; Paganin, D.M.; Siu, K.K.W. Quantitative single-exposure x-ray phase contrast imaging using a single attenuation grid. *Opt. Express* **2011**, *19*, 19781–19789. [[CrossRef](#)] [[PubMed](#)]
8. Pavlov, K.M.; Li, H.; Paganin, D.M.; Berujon, S.; Rougé-Labriet, H.; Brun, E. Single-Shot X-Ray Speckle-Based Imaging of a Single-Material Object. *Phys. Rev. Appl.* **2020**, *13*, 054023. [[CrossRef](#)]
9. Ruben, G.; Pinar, I.; Brown, J.M.C.; Schaff, F.; Pollock, J.A.; Crossley, K.; Maksimenko, A.; Hall, C.; Hausermann, D.; Uesugi, K.; et al. Full field X-ray Scatter Tomography. *arXiv* **2020**, arXiv:2012.09371.
10. Gureyev, T.E.; Paganin, D.M.; Arhatari, B.; Taba, S.T.; Lewis, S.; Brennan, P.C.; Quiney, H.M. Dark-field signal extraction in propagation-based phase-contrast imaging. *Phys. Med. Biol.* **2020**, *65*, 215029. [[CrossRef](#)]
11. Donnelley, M.; Morgan, K.S.; Gradl, R.; Klein, M.; Hausermann, D.; Hall, C.; Maksimenko, A.; Parsons, D.W. Live-pig-airway surface imaging and whole-pig CT at the Australian Synchrotron Imaging and Medical Beamline. *J. Synchrotron Radiat.* **2019**, *26*, 175–183. [[CrossRef](#)]
12. Morgan, K.S.; Parsons, D.; Cmielewski, P.; McCarron, A.; Gradl, R.; Farrow, N.; Siu, K.; Takeuchi, A.; Suzuki, Y.; Uesugi, K.; et al. Methods for dynamic synchrotron X-ray respiratory imaging in live animals. *J. Synchrotron Radiat.* **2020**, *27*, 164–175. [[CrossRef](#)]
13. Livingstone, J.; Adam, J.F.; Crosbie, J.C.; Hall, C.J.; Lye, J.E.; McKinlay, J.; Pelliccia, D.; Pouzoulet, F.; Prezado, Y.; Stevenson, A.W.; et al. Preclinical radiotherapy at the Australian Synchrotron’s Imaging and Medical Beamline: Instrumentation, dosimetry and a small-animal feasibility study. *J. Synchrotron Radiat.* **2017**, *24*, 854–865. [[CrossRef](#)]
14. Butler, D.J.; Stevenson, A.W.; Wright, T.E.; Harty, P.D.; Lehmann, J.; Livingstone, J.; Crosbie, J.C. High spatial resolution dosimetric response maps for radiotherapy ionization chambers measured using kilovoltage synchrotron radiation. *Phys. Med. Biol.* **2015**, *60*, 8625–8641. [[CrossRef](#)]
15. Yang, Y.; Crosbie, J.C.; Paiva, P.; Ibahim, M.; Stevenson, A.; Rogers, P.A.W. In Vitro Study of Genes and Molecular Pathways Differentially Regulated by Synchrotron Microbeam Radiotherapy. *Radiat. Res.* **2014**, *182*, 626–639. [[CrossRef](#)]
16. Stevenson, A.W.; Hall, C.J.; Mayo, S.C.; Hausermann, D.; Maksimenko, A.; Gureyev, T.E.; Nesterets, Y.I.; Wilkins, S.W.; Lewis, R.A. Analysis and interpretation of the first monochromatic X-ray tomography data collected at the Australian Synchrotron Imaging and Medical beamline. *J. Synchrotron Radiat.* **2012**, *19*, 728–750. [[CrossRef](#)]
17. Trinajstić, K.; Boisvert, C.; Long, J.; Maksimenko, A.; Johanson, Z. Pelvic and reproductive structures in placoderms (stem gnathostomes). *Biol. Rev.* **2015**, *90*, 467–501. [[CrossRef](#)]
18. Khosravani, M.R.; Reinicke, T. On the Use of X-ray Computed Tomography in Assessment of 3D-Printed Components. *J. Nondestruct. Eval.* **2020**, *39*, 75. [[CrossRef](#)]
19. Mehta, V.; Ahmad, N. Cone beamed computed tomography in pediatric dentistry: Concepts revisited. *J. Oral Biol. Craniofacial Res.* **2020**, *10*, 210–211. [[CrossRef](#)]
20. Stevenson, A.W.; Crosbie, J.C.; Hall, C.J.; Hausermann, D.; Livingstone, J.; Lye, J.E. Quantitative characterization of the X-ray beam at the Australian Synchrotron Imaging and Medical Beamline (IMBL). *J. Synchrotron Radiat.* **2017**, *24*, 110–141. [[CrossRef](#)]
21. Wypych, G. 1-Photophysics. In *Handbook of Material Weathering*, 6th ed.; Wypych, G., Ed.; ChemTec Publishing: Scarborough, ON, Canada, 2018; pp. 1–26. [[CrossRef](#)]
22. Yokhana, V.S.K.; Arhatari, B.D.; Gureyev, T.E.; Abbey, B. Soft-tissue differentiation and bone densitometry via energy-discriminating X-ray microCT. *Opt. Express* **2017**, *25*, 29328–29341. [[CrossRef](#)]
23. Ingal, V.N.; Beliaevskaya, E.A.; Brianskaya, A.P.; Merkurieva, R.D. Phase mammography—A new technique for breast investigation. *Phys. Med. Biol.* **1998**, *43*, 2555–2567. [[CrossRef](#)] [[PubMed](#)]
24. Snigirev, A.; Snigireva, I.; Kohn, V.; Kuznetsov, S.; Schelokov, I. On the possibilities of X-ray phase contrast microimaging by coherent high-energy synchrotron radiation. *Rev. Sci. Instrum.* **1995**, *66*, 5486–5492. [[CrossRef](#)]
25. Teague, M.R. Deterministic phase retrieval: A Green’s function solution. *J. Opt. Soc. Am.* **1983**, *73*, 1434–1441. [[CrossRef](#)]
26. Wilkins, S.W.; Gureyev, T.E.; Gao, D.; Pogany, A.; Stevenson, A.W. Phase-contrast imaging using polychromatic hard X-rays. *Nature* **1996**, *384*, 335–338. [[CrossRef](#)]
27. Nugent, K.A.; Gureyev, T.E.; Cookson, D.F.; Paganin, D.; Barnea, Z. Quantitative phase imaging using hard X rays. *Phys. Rev. Lett.* **1996**, *77*, 2961–2964. [[CrossRef](#)] [[PubMed](#)]
28. Arhatari, B.D.; De Carlo, F.; Peele, A.G. Direct quantitative tomographic reconstruction for weakly absorbing homogeneous phase objects. *Rev. Sci. Instrum.* **2007**, *78*, 053701. [[CrossRef](#)]

29. Gureyev, T.E.; Paganin, D.M.; Myers, G.R.; Nesterets, Y.I.; Wilkins, S.W. Phase and amplitude computer tomography. *Appl. Phys. Lett.* **2006**, *89*, 0341021–0341023. [[CrossRef](#)]
30. Gureyev, T.E.; Roberts, A.; Nugent, K.A. Partially Coherent Fields, The Transport-Of-Intensity Equation, And Phase Uniqueness. *J. Opt. Soc. Am. A* **1995**, *12*, 1942–1946. [[CrossRef](#)]
31. Paganin, D.; Mayo, S.; Gureyev, T.E.; Miller, P.R.; Wilkins, S.W. Simultaneous phase and amplitude extraction from a single defocused image of a homogeneous object. *J. Microsc.* **2002**, *206*, 33–40. [[CrossRef](#)]
32. Baran, P.; Pacile, S.; Nesterets, Y.I.; Mayo, S.C.; Dullin, C.; Dreossi, D.; Arfelli, F.; Thompson, D.; Lockie, D.; McCormack, M.; et al. Optimization of propagation-based x-ray phase-contrast tomography for breast cancer imaging. *Phys. Med. Biol.* **2017**, *62*, 2315–2332. [[CrossRef](#)]
33. Beltran, M.A.; Paganin, D.M.; Siu, K.K.W.; Fouras, A.; Hooper, S.B.; Reser, D.H.; Kitchen, M.J. Interface-specific x-ray phase retrieval tomography of complex biological organs. *Phys. Med. Biol.* **2011**, *56*, 7353–7369. [[CrossRef](#)] [[PubMed](#)]
34. Nesterets, Y.I.; Gureyev, T.E. Noise propagation in x-ray phase-contrast imaging and computed tomography. *J. Phys. D Appl. Phys.* **2014**, *47*, 105402. [[CrossRef](#)]
35. Paganin, D.; Nugent, K.A. Noninterferometric phase imaging with partially coherent light. *Phys. Rev. Lett.* **1998**, *80*, 2586–2589. [[CrossRef](#)]
36. Ferlay, J.; Soerjomataram, I.; Dikshit, R.; Eser, S.; Mathers, C.; Rebelo, M.; Parkin, D.M.; Forman, D.; Bray, F. Cancer incidence and mortality worldwide: Sources, methods and major patterns in GLOBOCAN 2012. *Int. J. Cancer* **2015**, *136*, E359–E386. [[CrossRef](#)]
37. Gureyev, T.E.; Nesterets, Y.I.; Baran, P.M.; Taba, S.T.; Mayo, S.C.; Thompson, D.; Arhatari, B.; Mihocic, A.; Abbey, B.; Lockie, D.; et al. Propagation-based x-ray phase-contrast tomography of mastectomy samples using synchrotron radiation. *Med. Phys.* **2019**, *46*, 5478–5487. [[CrossRef](#)] [[PubMed](#)]
38. Gureyev, T.E.; Mayo, S.C.; Myers, D.E.; Nesterets, Y.; Paganin, D.M.; Pogany, A.; Stevenson, A.W.; Wilkins, S.W. Refracting Röntgen’s rays: Propagation-based X-ray phase contrast for biomedical imaging. *J. Appl. Phys.* **2009**, *105*, 102005. [[CrossRef](#)]
39. Kitchen, M.J.; Buckley, G.A.; Gureyev, T.E.; Wallace, M.J.; Andres-Thio, N.; Uesugi, K.; Yagi, N.; Hooper, S.B. CT dose reduction factors in the thousands using X-ray phase contrast. *Sci. Rep.* **2017**, *7*, 15953. [[CrossRef](#)] [[PubMed](#)]
40. Gureyev, T.E.; Nesterets, Y.I.; Kozlov, A.; Paganin, D.M.; Quiney, H.M. On the “unreasonable” effectiveness of transport of intensity imaging and optical deconvolution. *J. Opt. Soc. Am. A* **2017**, *34*, 2251–2260. [[CrossRef](#)] [[PubMed](#)]
41. Mayo, S.C.; Miller, P.R.; Wilkins, S.W.; Davis, T.J.; Gao, D.; Gureyev, T.E.; Paganin, D.; Parry, D.J.; Pogany, A.; Stevenson, A.W. Quantitative X-ray projection microscopy: Phase-contrast and multi-spectral imaging. *J. Microsc.* **2002**, *207*, 79–96. [[CrossRef](#)] [[PubMed](#)]
42. Specification for Hamamatsu C10900D Detector. Available online: <https://dtsheet.com/doc/569688/hamamatsu-c10900d> (accessed on 21 April 2021).
43. Specification for Xineos 3030HR Detector. Available online: <https://www.teledynedalsa.com/en/products/imaging/medical-x-ray-detectors/xineos-large-area/xineos-3030hr/> (accessed on 21 April 2021).
44. Gureyev, T.; Nesterets, Y.; Ternovski, D.; Thompson, D.; Wilkins, S.; Stevenson, A.; Sakellariou, A.; Taylor, J. Toolbox for Advanced X-ray Image Processing. In Proceedings of the Advances in Computational Methods for X-ray Optics II, San Diego, CA, USA, 21–24 August 2011.
45. Marone, F.; Stampanoni, M. Regridding reconstruction algorithm for real-time tomographic imaging. *J. Synchrotron Radiat.* **2012**, *19*, 1029–1037. [[CrossRef](#)] [[PubMed](#)]
46. Marcou, J.; Bosworth, R.; Clarken, R.; Martin, P.; Moll, A. ASCI: A Compute platform for researchers at the Australian Synchrotron. In Proceedings of the 16th International Conference on Accelerator and Large Experimental Physics Control Systems (ICALEPCS 2017), Barcelona, Spain, 8–13 October 2017.
47. Tavakoli Taba, S.; Arhatari, B.D.; Nesterets, Y.I.; Gadomkar, Z.; Mayo, S.C.; Thompson, D.; Fox, J.; Kumar, B.; Prodanovic, Z.; Hausermann, D.; et al. Propagation-Based Phase-Contrast CT of the Breast Demonstrates Higher Quality Than Conventional Absorption-Based CT Even at Lower Radiation Dose. *Acad. Radiol.* **2021**, *28*, e20–e26. [[CrossRef](#)] [[PubMed](#)]
48. Gureyev, T.; Mohammadi, S.; Nesterets, Y.; Dullin, C.; Tromba, G. Accuracy and precision of reconstruction of complex refractive index in near-field single-distance propagation-based phase-contrast tomography. *J. Appl. Phys.* **2013**, *114*, 1–10. [[CrossRef](#)]
49. Born, M.; Wolf, E. *Principles of Optics*, 7th ed.; Cambridge University Press: Cambridge, UK, 1999.